

Automatic Optic Disc Detection in OCT Slices via Low-Rank Reconstruction

Huazhu Fu*, Dong Xu, Stephen Lin, Damon Wing Kee Wong, and Jiang Liu

Abstract—Optic disc measurements provide useful diagnostic information as they have correlations with certain eye diseases. In this paper, we provide an automatic method for detecting the optic disc in a single OCT slice. Our method is developed from the observation that the retinal pigment epithelium (RPE) which bounds the optic disc has a low-rank appearance structure that differs from areas within the disc. To detect the disc, our method acquires from the OCT image an RPE appearance model that is specific to the individual and imaging conditions, by learning a low-rank dictionary from image areas known to be part of the RPE according to priors on ocular anatomy. The edge of the RPE, where the optic disc is located, is then found by traversing the retinal layer containing the RPE, reconstructing local appearance with the low-rank model, and detecting the point at which appearance starts to deviate (i.e., increased reconstruction error). To aid in this detection, we also introduce a geometrical constraint called the distance bias that accounts for the smooth shape of the RPE. Experiments demonstrate that our method outperforms other OCT techniques in localizing the optic disc and estimating disc width. Moreover, we also show the potential usage of our method on optic disc area detection in 3-D OCT volumes.

Index Terms—Layer segmentation, optic disc detection, optical coherence tomography (OCT).

I. INTRODUCTION

THE location where ganglion cell axons exit in the eye to form the optic nerve is called the optic disc [1], [2]. Since the measurement of the optic disc is important for many medical applications such as glaucoma screening [3] and large exudative lesion analysis [4], there has been much recent effort on automatically detecting the optic disc in ocular images. Many existing optic disc detection methods focus on segmenting the optic disc region in fundus images [5]–[8]. For example, Xu *et al.* [9] employed the deformable model technique through minimization of an energy function to detect the disc. Cheng *et al.* [8] considered optic disc detection as a superpixel classification problem based on center-surround statistics. The method of Morales *et al.* [10] extracted the optic disc contour based on

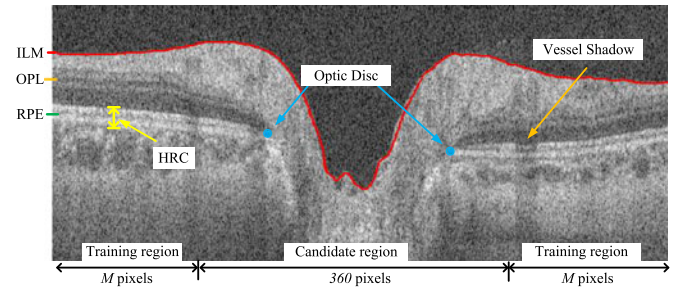


Fig. 1. Optic nerve head structure in a cropped OCT slice. The red curve denotes the ILM boundary. The boundary points of the optic disc, marked by blue points, are located at the endpoints of the RPE layer. ILM: Inner limiting membrane. OPL: Outer plexiform layer. RPE: Retinal pigment epithelium fused with Bruch's membrane and choriocapillaris. HRC: Hyper reflective complex.

mathematical morphology and principal components analysis. However, a major problem of these methods is that they easily fail when the optic disc does not have a distinct color in the fundus image.

A relatively new imaging technique called optical coherence tomography (OCT) provides a clearer view of intraretinal morphology and enables noninvasive depth-resolved functional imaging of the retina [11]. In an OCT slice, the boundary of the optic disc appears at the end of the retinal pigment epithelium (RPE) [12]–[14], as shown in Fig. 1. Some OCT-based optic disc detection methods operate on 3-D OCT volumes [15]–[19]. For example, Lee *et al.* [18] extracted intraretinal surfaces from 3-D OCT volumes, and classifies the optic disc, cup, and neuroretinal rim using a k-NN classifier. Miri *et al.* [19] provided a multimodal pixel-classification approach to segment the optic disc by combining information from stereo fundus images and an OCT volume. However, acquisition of numerous OCT slices for 3-D reconstruction is susceptible to misalignment error due to eye movement. Although 3-D volume scanning acquisition is becoming more common with advances in OCT technology, examination of a single B-scan for optic disc detection remains an important problem in practice for routine clinical applications. In the state-of-the-art method for optic disc detection from a single OCT slice, Boyer *et al.* [20] extracted Hadamard transform features along a retinal layer containing the RPE, and grouped the features into two clusters to identify the optic disc endpoints. However, feature-based clustering can be sensitive to appearance variations due to noise and blood vessel shadows in the OCT image. Moreover, the method in [20] does not take advantage of the smooth geometric structure of the RPE in localizing the optic disc endpoints.

In this paper, we present a general technique for optic disc detection in a single OCT slice via low-rank reconstruction.

Manuscript received May 31, 2014; revised August 5, 2014 and October 10, 2014; accepted October 28, 2014. Date of publication November 26, 2014; date of current version March 17, 2015. This work was supported by the Singapore A*STAR SERC under Grant 112-148-0003. Asterisk indicates corresponding author.

*H. Fu is with the School of Computer Engineering, Nanyang Technological University, 639798 Singapore, Singapore (e-mail: hzfu@ntu.edu.sg).

D. Xu is with the School of Computer Engineering, Nanyang Technological University.

S. Lin is with Microsoft Research.

D. W. K. Wong and J. Liu are with the iMED Ocular Imaging Program, Institute for Infocomm Research, Agency for Science, Technology and Research.

Color versions of one or more of the figures in this paper are available online at <http://ieeexplore.ieee.org>.

Digital Object Identifier 10.1109/TBME.2014.2375184

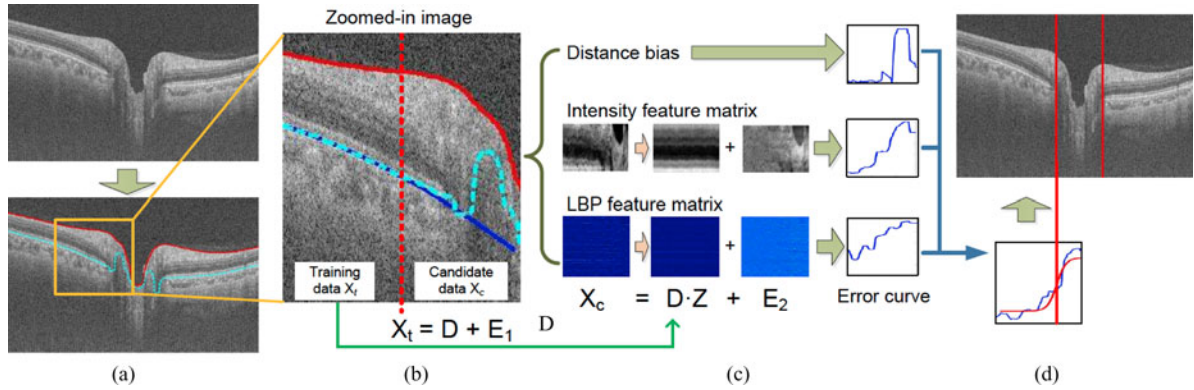


Fig. 2. Illustration of our approach. (a) Our method first segments the retinal layers and divides the region into a training region and a candidate region. The red and cyan curves denote the boundaries of ILM layer and the segmented RPE layer, respectively. (b) Then the low-rank dictionary is learned from the training data. (c) We next reconstruct the layer appearance at points along the candidate region, and output the reconstruction error curves based on intensity and LBP features as well as the distance bias curve. (d) Finally, the optic disc boundary points are detected by combining these three error curves.

Based on retinal structure priors, we divide the pixels along the RPE layer boundary into training data and optic disc edge candidates. A low-rank dictionary is learned from the training data to reconstruct candidate pixels, and the reconstruction error is used to identify the beginning of the optic disc. The main contributions of this paper are as follows: 1) We present an optic disc detection method via low-rank reconstruction, where learning of the low-rank dictionary is beneficial for handling noise and vessel shadows in OCT slices. 2) The reconstruction process does not rely on pre-labeled training samples. The training data is extracted from the single given OCT slice itself using retinal structure priors. 3) A geometrical constraint that accounts for the smooth shape of the RPE, called the distance bias, is provided to improve accuracy. 4) Our method not only obtains encouraging performance in localizing the optic disc and estimating disc width from a single OCT slice, but also has potential for optic disc area detection in 3-D OCT volumes.

II. OUR APPROACH

Our method first segments the retinal layer boundaries containing the inner limiting membrane (ILM) and RPE. As shown in the framework of our method in Fig. 2, the segmented layer boundary (cyan dashed curve) not only includes the RPE but also extends into the optic disc. The segmented boundary is then divided into two parts: A training region for learning a low-rank appearance model of the RPE, and a candidate region along which the optic disc boundary will be searched. The training and candidate regions are divided according to structural priors for the optic nerve head (ONH), which indicate parts of the layer that are certain to belong to the RPE. In the training region, a low-rank dictionary based on intensity features and local binary patterns (LBP) is learned for vertical slices along the RPE. The dictionary is then used to reconstruct layer appearance at points along the candidate region, with the reconstruction errors recorded as error curves. In addition, an error curve is constructed based on distance bias, which represents deviations from the smooth geometrical structure extrapolated from the known RPE pixels in the training region (blue solid curve). From a combination of these error curves, the optic disc boundary points are detected.

The OCT slices in our paper are obtained by using a TOPCON DRI OCT-1 Atlantis swept source OCT imaging device, which has a depth resolution of $8 \mu\text{m}/\text{pixel}$ and lateral resolution of $10 \mu\text{m}/\text{pixel}$. A slice consists of 1024 A-scans (columns) each with 992 pixels.

A. Retinal Layer Boundary Segmentation

While there exist methods for extracting multiple retinal layers from OCT slices [21]–[23], only the RPE and ILM layer boundaries are needed in our paper. These two layers have specific characteristics that distinguish them from the surrounding areas and layers. We can, thus, employ a fast and simple method to extract the ILM and RPE layer boundaries from an OCT slice.

1) *ILM Layer Boundary Segmentation*: The ILM is defined as the boundary between the retina and the vitreous body, which is the first boundary in the OCT slice as shown in Fig. 1. After reducing the speckle noise of the OCT slice with a 2-D Gaussian filter, we threshold the OCT slice by using Otsu's method [24], as shown in Fig. 3(b). Then, the topmost binary edge is selected as the ILM layer, as indicated by the red boundary in Fig. 3(d). The lowest point on the ILM layer boundary is used to approximately localize the ONH center.

2) *RPE Layer Boundary Segmentation*: In general, the two strongest gradient edges in the vertical direction of each column of the OCT slice corresponds to the ILM (upper) and RPE (lower) layer boundaries, as shown in Fig. 3(c). After extracting the ILM layer boundary, we can take the strongest gradient edge below the ILM layer as the RPE layer boundary. To elevate the robustness of the RPE layer boundary segmentation, our method employs three steps. First, a 2-D Gaussian filter is used to reduce speckle noise in the OCT slice. Then, we select one point in each column of the OCT slice that is below the ILM layer and has the strongest positive vertical gradient. Finally, we connect these points as the RPE layer boundary, and employ a 1-D median filter [25] to smooth its vertical position in each column. Note that the extracted RPE layer extends across the entire OCT slice, including the non-RPE part, as shown by the cyan curve in Fig. 3(d). Thus, we will use the extracted RPE layer boundary as a starting point along which we will identify the true endpoint of the RPE, and hence locate the boundary of the optic disc.

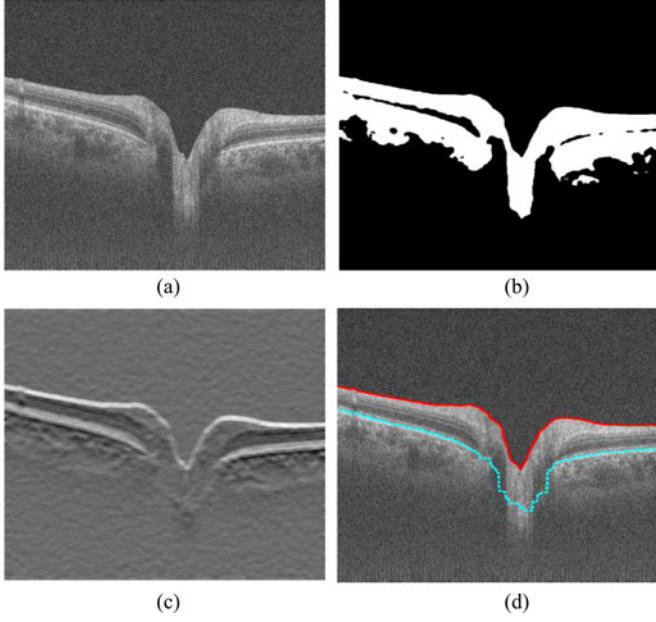


Fig. 3. Layer boundary segmentation. (a) Input OCT slice. (b) Thresholded OCT slice. (c) Vertical gradient map. (d) ILM (red curve) and RPE (cyan curve) layer boundaries segmentation result.

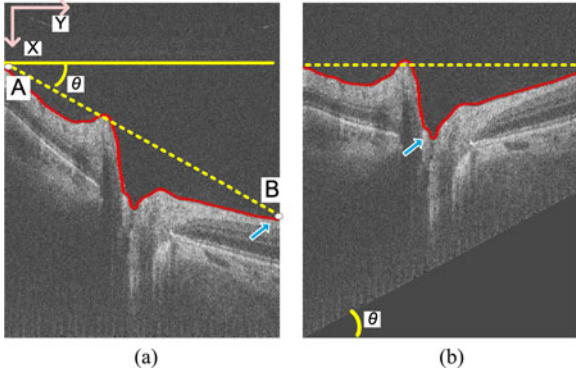


Fig. 4. ONH-centered OCT slice preprocessing, where the red curve denotes the detected ILM layer boundary. (a) Original OCT slice may exhibit a sloping retina, such that the lowest ILM point (blue arrow) deviates from the ONH. Points A and B are the endpoints of the ILM layer boundary in the OCT slice, and the dashed yellow line connecting the endpoints A and B denotes the plane of the ILM layer. The solid yellow line indicates a horizontal line, and θ is the angle of inclination. (b) After preprocessing, the plane of the ILM layer is horizontal, and the lowest ILM point is located in the ONH.

3) *ONH Localization*: In our method, the ONH is employed as a landmark to define the training region and the candidate region. Generally, the lowest point on the ILM layer boundary could be used to locate the ONH. However, some OCT slices may exhibit serious sloping of the retina, such that the lowest ILM point is not in the ONH, as shown in Fig. 4(a). For these OCT slices, we employ a preprocessing step to correct this sloping. First, we compute the inclination angle θ of the retina in the OCT slice from the edge points of the ILM layer, e.g., points A and B in Fig. 4(a). Then, the corrected coordinate (\hat{x}, \hat{y}) for the point at (x, y) is obtained through a rotation with a fixed y value

$$(\hat{x}, \hat{y}) = (y \tan(\theta) + x, y). \quad (1)$$

Fig. 4(b) shows the corrected OCT slice, where the lowest ILM point is located in the ONH.

B. Low-Rank Dictionary Learning

The optic disc boundary points are defined as the left/right endpoints of the RPE, which are detected separately in our paper. It has been observed that the regions along the RPE layer boundary, including the OPL and hyper reflective complex (HRC) as shown in Fig. 1, have a consistent retinal structure that includes multiple surrounding bands, while the regions beyond the RPE endpoints are different [26]. This observation motivates our use of low-rank reconstruction for detecting RPE endpoints. Toward this end, we construct a low-rank dictionary from the training region to model the RPE appearance, and then use the low-rank dictionary to detect the optic disc point in the candidate region based on changes in low-rank reconstruction error.

To divide the segmented layer into the training and candidate regions, we make use of prior knowledge that the optic disc is approximately centered at the ONH and has a vertical and horizontal diameter of about 1.92 ± 0.29 mm and 1.76 ± 0.31 mm [27], [28]. Based on this, we define a loose candidate region as having a 360-pixel width (corresponding to about 2.8 mm) centered horizontally on the lowest ILM point. The remaining part of the segmented layer is taken as the training region. We denote the width of the training region as M , which is also called dictionary size in this work. As the training data is derived from the input image itself, the learned model is specifically tailored to the individual and the imaging apparatus used to capture the OCT image. A set of labeled training images is not required.

We extract appearance features along each pixel of the training region, and arrange them into a feature matrix \mathbf{X}_t . Because of the consistent retinal structure along the RPE layer boundary, the feature matrix \mathbf{X}_t can be decomposed into a low-rank matrix \mathbf{D} and sparse errors \mathbf{E}_1 by using the recent work robust principal components analysis (RPCA) [29]:

$$\begin{aligned} \{\hat{\mathbf{D}}, \hat{\mathbf{E}}_1\} &= \arg \min_{\mathbf{D}, \mathbf{E}_1} \|\mathbf{D}\|_* + \lambda_1 \|\mathbf{E}_1\|_1 \\ \text{s.t. } \mathbf{X}_t &= \mathbf{D} + \mathbf{E}_1 \end{aligned} \quad (2)$$

where $\|\cdot\|_*$ denotes the nuclear norm, $\|\cdot\|_1$ denotes the ℓ_1 norm, and \mathbf{X}_t is the feature matrix which is decomposed into the low-rank dictionary \mathbf{D} and sparse error matrix \mathbf{E}_1 . The optimal solution $\{\hat{\mathbf{D}}, \hat{\mathbf{E}}_1\}$ can be solved by using the inexact augmented Lagrange multiplier (inexact ALM) [31] algorithm in [29].

C. Low-Rank Reconstruction

With the learned low-rank dictionary $\hat{\mathbf{D}}$, the feature matrix of the candidate region will be reconstructed to obtain the reconstruction error. Based on the low-rank representation (LRR) [30], we seek a low-rank reconstruction coefficient matrix $\hat{\mathbf{Z}}$ and the corresponding reconstruction error matrix $\hat{\mathbf{E}}_2$, by solving the

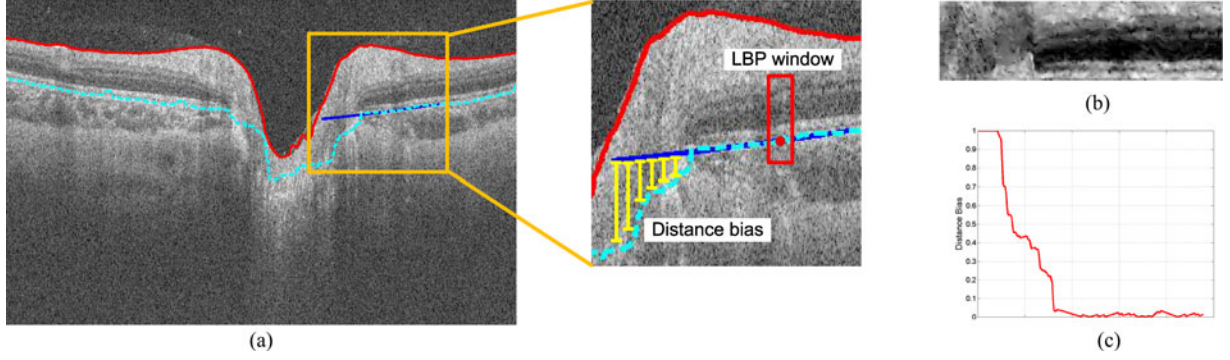


Fig. 5. Features and distance bias. (a) LBP window (red box) and distance bias (yellow bars). The red, cyan and blue curves denote the ILM layer boundary, the segmented RPE layer boundary and the fitted curve for calculating distance bias, respectively. (b) Intensity feature matrix. (c) Distance bias curve of (a).

following problem

$$\begin{aligned} \{\hat{\mathbf{Z}}, \hat{\mathbf{E}}_2\} &= \arg \min_{\mathbf{Z}, \mathbf{E}_2} \|\mathbf{Z}\|_* + \lambda_2 \|\mathbf{E}_2\|_{2,1} \\ \text{s.t. } \mathbf{X}_c &= \hat{\mathbf{D}}\mathbf{Z} + \mathbf{E}_2 \end{aligned} \quad (3)$$

where \mathbf{X}_c denotes the feature matrix of the candidate region, which is represented as the sum of $\hat{\mathbf{D}}\mathbf{Z}$ and \mathbf{E}_2 . Moreover, minimizing $\|\mathbf{E}_2\|_{2,1}$ encourages column-sparsity in \mathbf{E}_2 , where $\|\cdot\|_{2,1}$ is the $\ell_{2,1}$ norm used in [30]. The underlying assumption here is that image corruptions are sample-specific, some data (i.e., columns in \mathbf{X}_c) are corrupted by vessel shadows. The optimal solution $\{\hat{\mathbf{Z}}, \hat{\mathbf{E}}_2\}$ can be obtained by using the inexact ALM algorithm in [30].

To normalize $\hat{\mathbf{E}}_2$, we rescale $\hat{\mathbf{E}}_2$ as $\hat{\mathbf{E}}_2 = \hat{\mathbf{E}}_2 / \|\mathbf{X}_c\|_F$, where $\|\cdot\|_F$ denotes the Frobenius norm [32]. After that, we generate the reconstruction error curve by calculating the ℓ_2 norm of each column of $\hat{\mathbf{E}}_2$. In this error curve, the points from the RPE are expected to have low-value errors, since those points are ideally well-reconstructed. In contrast, the points outside the RPE tend to have high errors.

D. Features and Distance Bias

Technically, any feature could be employed in our method to describe pixels in the RPE layer. However, features whose range can cover the OPL and HRC are preferable, since the OPL and HRC are stable and consistent along the RPE layer and are thus helpful for determining the endpoint of the RPE layer. In our method, we employ two types of features: intensity values and LBP [33]. The intensity values are specifically a vector of pixel intensities in the OCT image from 20 rows below each point on the segmented boundary to 60 rows above it. Together, the intensity vectors form an intensity feature matrix, illustrated in Fig. 5(b). The second feature, LBP, is widely-used for many applications. In this paper, we use a 10×5 block within a 80×10 window around each extracted RPE layer boundary point, with the boundary located 25% from the bottom as shown within the red box in Fig. 5(a). The extracted LBP feature vectors are collected into an LBP feature matrix.

Moreover, we also introduce a geometrical constraint called distance bias in our method. The RPE is identified as a smooth, convex surface composed of a single layer of hexagonal cells that help to maintain the integrity of the barrier between the choroid

and the retina [34]. We empirically found that the smooth shape of the RPE can be well approximated by a quadratic curve. A quadratic curve is, thus, fitted to the RPE layer boundary by linear least squares in the training region and used to constrain the endpoint position in the candidate region. Based on this constraint, we define distance bias as the vertical distance between the fitted curve and the RPE layer boundary in the candidate region, as illustrated in Fig. 5(a) by yellow bars. From the distance bias, we obtain a geometrical error curve, as shown in Fig. 5(c).

E. Optic Disc Localization

The error curves for intensity, LBP, and distance bias are combined by normalizing the curves and computing their sum. By treating the three factors separately until now, the issue of normalizing different features within a single-feature matrix has been avoided. In the aggregated error curve, points that belong to the RPE layer should have low error, while other points within the optic disc will have higher errors. The optic disc point should lie between the corresponding two parts of the segmented layer. To identify this point, we fit a sigmoid function to the error curve and use its midpoint to locate the optic disc boundary as shown in Fig. 2(d). We have found this approach to give an accurate estimate of the optic disc position.

III. EXPERIMENTS

For testing our method, we collect OCT slices centered at the ONH from 20 normal persons, four of whom were selected randomly for recapture of their OCT slices after a long time interval (more than six months). This dataset, thus, consists of 48 OCT slices in total. These slices were captured by using the 2-D imaging protocol, at 1024×992 image resolution and with a depth resolution of $8 \mu\text{m}/\text{pixel}$ and lateral resolution of $10 \mu\text{m}/\text{pixel}$. A trained labeler marked the ground-truth optic disc points manually in each of the images, and two experts examined the ground-truth labelings for quality control. We set the parameter $\lambda_1 = 0.35$ in RPCA, the parameter $\lambda_2 = 0.45$ in LRR, and the dictionary size $M = 140$ as the default parameters for all the experiments.

Our evaluation employs two error metrics. The first is the distance error in terms of image columns between the detected optic disc and the groundtruth: $m_d = |C_d - C_{gt}|$, where C_d and

TABLE I
PERFORMANCES (AVERAGE \pm STANDARD DEVIATIONS)
OF VARIOUS OPTIC DISC DETECTION METHODS

	m_d (pixel)	m_w (%)
Baseline 2-D	25.8 \pm 23.1	19.2 \pm 16.4
Boyer <i>et al.</i> [20]	20.7 \pm 19.8	18.0 \pm 14.0
Intensity	22.2 \pm 20.8	14.7 \pm 12.8
LBP	24.4 \pm 17.7	20.5 \pm 14.2
Distance bias	21.4 \pm 18.4	18.3 \pm 12.2
Intensity + LBP	18.6 \pm 17.7	12.2 \pm 9.7
Intensity+ Distance	16.1 \pm 14.5	11.2 \pm 9.1
LBP + Distance	14.8 \pm 12.9	8.9 \pm 7.6
w/o Dictionary	18.1 \pm 15.9	12.7 \pm 10.7
Our method	12.4 \pm 12.1	7.9 \pm 8.4

C_{gt} denote the column coordinates of the detected and ground-truth optic disc. The second measure is the width error ratio: $m_w = |W_d - W_{gt}|/W_{gt}$, where W_d and W_{gt} denote the detected and ground-truth optic disc widths.

A. Optic Disc Detection Performance

We evaluate the optic disc detection performance of our method through comparisons to simplified versions of our method with only a subset of the features and to other techniques: 1) each of the three features alone (“intensity”, “LBP”, and “distance bias”), where the final localization curve is generated by using only one error curve; 2) a combination of only two features (“intensity + LBP”, “intensity + distance”, and “LBP + distance”); 3) our full method without dictionary learning (“w/o Dictionary”) i.e., we directly use the candidate data itself as a *self-expressive* dictionary [30] for the LRR in (3); 4) the existing method for optic disc detection in a single OCT slice (“Boyer *et al.* [20]”); 5) a baseline method that detects the optic disc based on the average intensity of the RPE layer boundary (“Baseline 2-D”), which takes advantage of the fairly large contrast that appears at the endpoint of the RPE layer. Table I shows the performances (average \pm standard deviations) of the various optic disc detection methods.

In Table I, it can be seen that the combination of intensity and LBP (“intensity + LBP”) generally outperforms each of the features individually. Adding the distance bias feature to LBP leads to an improvement of about 12% in the term of width error ratio m_w , which indicates the benefit of accounting for distance bias. In Table 1, the results of our method without dictionary learning (w/o Dictionary”) are also reported, in which the candidate data itself serves as the dictionary for the LRR. Since the candidate data contains regions both with and without the RPE layer, the dictionary learned from it does not have the low-rank property. As a result, the reconstruction error provides only a weak indicator of the endpoint of the RPE layer. The low-rank dictionary learning step in the proposed method makes the reconstruction more robust and effective by removing spurious outliers such as heavy noise and vessel shadows from the OCT slice. This is different from the baseline techniques “Boyer *et al.* [20]” and “Baseline 2-D”, which directly cluster pixels via the extracted features that can be distorted by outlier elements.

Fig. 6 displays some detection results, where the red, green, and yellow lines indicate our results, those of “Boyer *et al.* [20]” and the groundtruth, respectively. Our method generally outperforms “Boyer *et al.* [20]”. In the figure, the blue dashed lines mark the RPE layer segmented according to Gaussian filter responses. The segmentations include the RPE as well as non-RPE extensions into the optic disc. In many cases, the geometrical constraint from distance bias provides a useful detection cue. However, for some cases, non-RPE points in the layer may satisfy the distance bias constraint. Our detection relies more on intensity and LBP features in these cases.

We performed our experiments using a PC with a 3.2 GHz CPU and 16 GB RAM. The code is implemented in MATLAB without optimization. Fig. 7 shows the computation time (in seconds) of our entire method (red curve) and of its main steps including feature extraction (green), dictionary learning via RPCA (blue), and reconstruction via LRR (black). Feature extraction and dictionary learning require the most computation in our method. The computation time of the dictionary learning procedure increases consistently with the dictionary size M . Typically, our method takes about 50 s for an OCT slice of the image resolution 1024×992 .

B. Optic Disc Area Detection in the OCT Volume

Although we focus on optic disc detection from a single OCT slice, our method can be extended to handle an OCT volume. For a 3-D OCT volume, we first find the OCT slices that cross the ONH, determined by the height of the ILM layer within the training region as shown in Fig. 8(a). We employ a height threshold t ($t = 100$ in our experiment) to select the OCT slices, and then detect the optic disc in each single OCT slice by using our method. Finally, a fitted ellipse [35] is computed as the disc boundary on the OCT fundus image, as shown in Fig. 8(c).

For testing our method on OCT volumes, we collect seven OCT volumes (each of $992 \times 512 \times 512$ resolution) by using the 3-D imaging protocol. The ground-truth optic disc boundary of a 3-D OCT volume is obtained by first manually labeling the optic disc points in each ONH-centered slice in the same manner as that for 2-D OCT slice labeling (with a trained labeler and two experts for quality control). These labeled points are then fit with an ellipse to generate the ground-truth optic disc boundary.

We compare our method with four other techniques. The first two, namely “Boyer *et al.* [20]” and “Baseline 2-D”, use the detection methods for single OCT slices and then fit an ellipse to the detected points to find the detected optic disc area in the 3-D OCT volume, similar to our method. The third method is based on Lee *et al.* [18], which operates on 3-D OCT volumes. Note that Lee *et al.* [18] involves kNN classification, which is not applicable to our unsupervised setting without labeled training data. Thus, we modify the last step in Lee *et al.* [18] to make it unsupervised. We extract the RPE surface from the 3-D OCT volume and flatten the surface. Then a binary clustering method is applied based on the features (e.g., intensity and gradient features) extracted from the RPE surface to determine the optic disc region. We refer to this modification of Lee *et al.* [18] as “Baseline 3-D”. The fourth baseline method is our implementation of Ishikawa *et al.* [17], which detects the optic disc area in

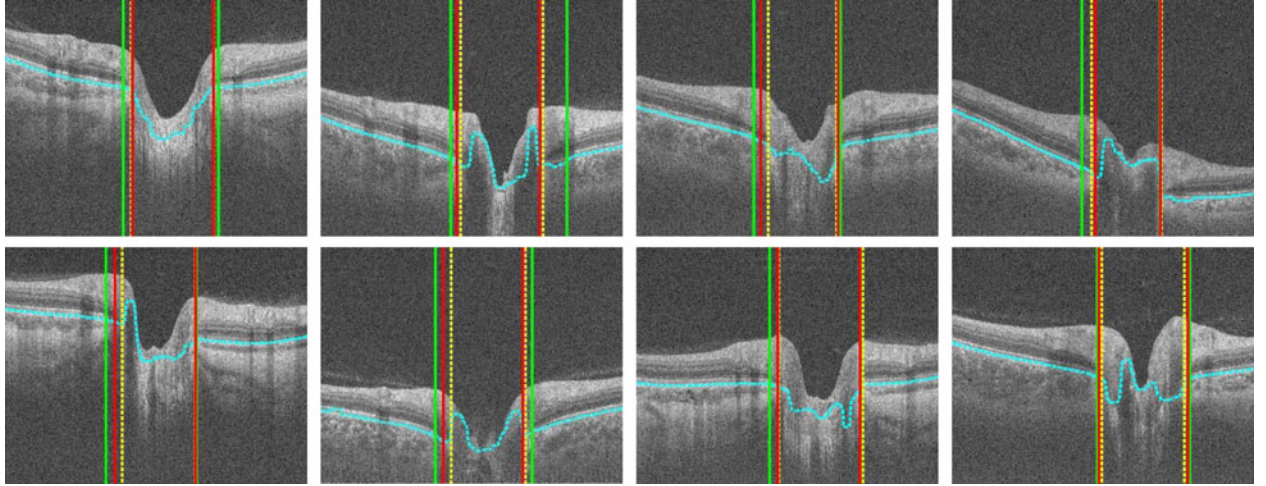


Fig. 6. Optic disc detection results of different methods (only a rectangular region around the ONH is shown). The cyan dashed curve denotes the segmented RPE layer boundary, and the red, green and yellow lines indicate the detection locations for our method, Boyer *et al.* [20], and the groundtruth, respectively.

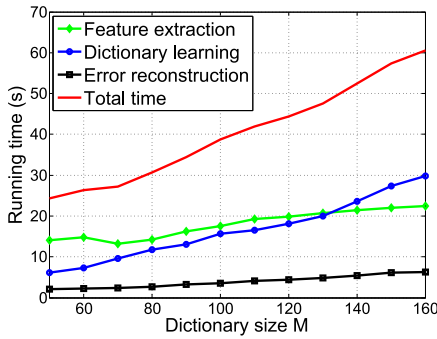


Fig. 7. Computation times with respect to different dictionary sizes.

TABLE II
PERFORMANCES (AVERAGE \pm STANDARD DEVIATIONS) OF VARIOUS
OPTIC DISC DETECTION METHODS ON 3-D OCT VOLUMES.

	m_1 (%)	m_2 (%)
Baseline 2-D	22.6 ± 12.3	20.2 ± 16.1
Boyer <i>et al.</i> [20]	20.1 ± 9.6	17.9 ± 10.4
Ishikawa <i>et al.</i> [17]	21.9 ± 11.6	18.3 ± 15.4
Baseline 3-D	19.7 ± 10.6	16.5 ± 9.9
Our method	16.2 ± 6.6	12.6 ± 7.9

a 3-D OCT volume by using the modified active contour model [5].

For OCT volumes, we employ two evaluation criteria to measure disc region detection accuracy. The first measure is the nonoverlap ratio: $m_1 = 1 - \frac{\text{Area}(R \cap R_{GT})}{\text{Area}(R \cup R_{GT})}$, where R and R_{GT} denote the detected optic disc region and the ground-truth ellipse, respectively. The second measure is the relative absolute area difference: $m_2 = \frac{|\text{Area}(R) - \text{Area}(R_{GT})|}{\text{Area}(R_{GT})}$. Table II shows the performances (average \pm standard deviations) of our method and other methods, and Fig. 9 displays the optic disc detection results on an OCT volume, where the top row is the disc area detection results on the OCT fundus images and the bottom row shows the corresponding OCT slice results. The red, green, blue, and yellow lines indicate the detection results from our method,

Ishikawa *et al.* [17], “Baseline 3-D” and the groundtruth, respectively.

The “Baseline 2-D” method does not work well, since poor performance on single OCT slices leads to distorted disc regions. “Boyer *et al.* [20]” and “Ishikawa *et al.* [17]” obtain similar performance. “Baseline 3-D” generates stable and regular disc regions, but it depends on accurate OCT surface flattening to reduce the influence of fore-aft eye movement. Furthermore, it tends to produce the results with smaller disc sizes than the groundtruth, such as the blue curves in the third column of Fig. 9. In contrast, by taking the advantages of processing single OCT slices, our method detects the endpoints of the RPE layer more accurately and outperforms the existing methods. Moreover, in contrast to a single OCT slice, an OCT volume with a fitted ellipse essentially provides a smooth neighborhood constraint, which is beneficial for removing outliers introduced by disc detection errors on a small number of OCT slices.

C. Discussion

In this paper, we present a technique for optic disc detection without also addressing the problem of optic cup detection, though it is also needed for computing the cup-to-disc ratio, the most commonly used clinical feature in glaucoma diagnosis. While investigating optic cup detection in a similar fashion would be an interesting and important study, optic disc detection nevertheless remains an important problem itself as it is often used to support other detection and assessment tasks. Fully/semiautomated quantitative disc assessment using ocular imaging devices (for fundus images and OCT volumes) usually starts with detecting the optic disc margin [13]. The optic disc margin also provides a fundamental landmark for detecting other retinal parts. For example, optic cup detection is generally performed based on an assumption that optic cup is only within the disc area [7], [8]. Typically in an OCT slice, the optic cup diameter is defined as the length of the line that connects the outermost borders of the cup at the level of $150 \mu\text{m}$ above the optic disc reference line [1], [12]. Thus, optic disc detection is essential for accurate optic cup detection.

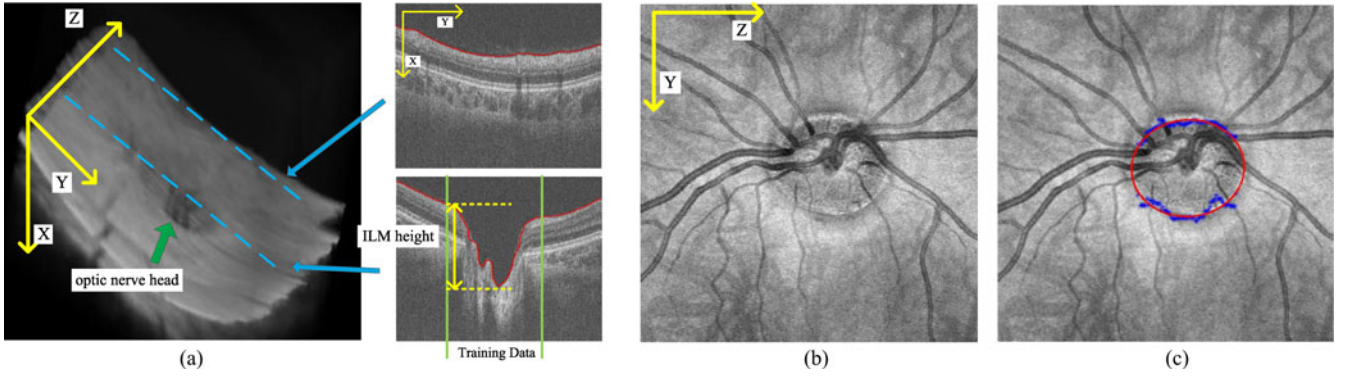


Fig. 8. Optic disc detection in 3-D OCT volumes. (a) In a 3-D OCT volume, OCT slices containing the ONH (bottom-left) have a larger ILM height within the training region than the other slices (upper-left). (b) The OCT fundus image generated by averaging intensity values of each A-scan. (c) Our optic disc detection result, where the blue points are the detected disc from individual OCT slices, and the red line is the fitted ellipse.

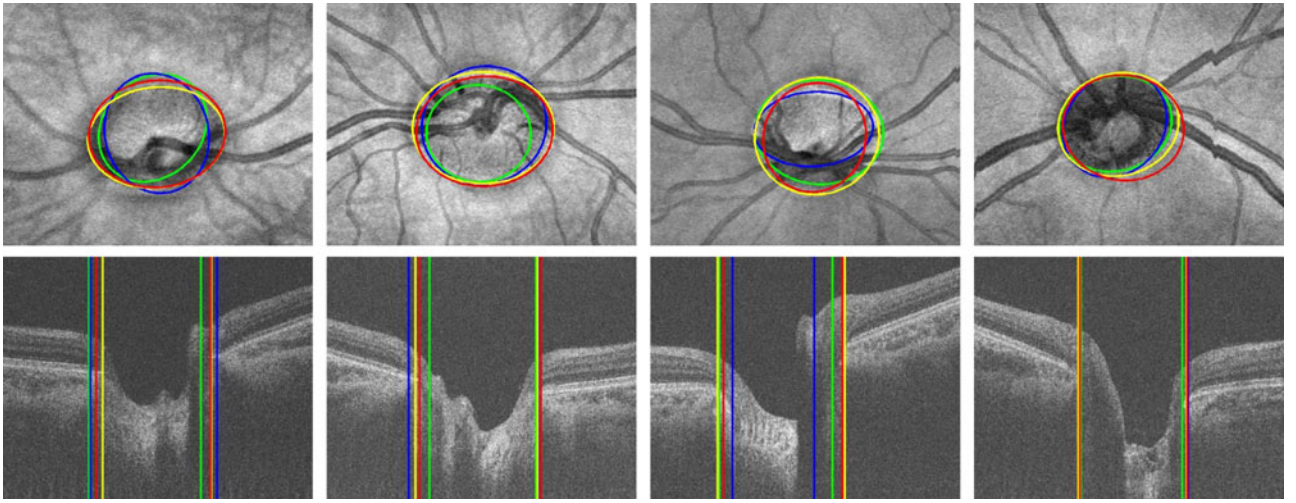


Fig. 9. Optic disc detection results on OCT volumes (only a rectangular region around the ONH is shown). The top row shows disc area detection results on OCT fundus images, and the bottom row displays the corresponding OCT slice results on the ONH. The red, green, blue, and yellow lines indicate the detection results of our method, Ishikawa *et al.* [17], Baseline 3-D, and the groundtruth, respectively.

A limitation of our paper is that experiments on glaucoma patients were not included. We note, however, that for some retinal diseases such as glaucoma, the early changes in the optic disc are subtle [36], [37], such that the structure prior for dividing the training and candidate regions in our method remain valid. Though we did not provide an evaluation of glaucoma diagnosis, our disc detection method outperforms the other methods by nearly 10% in width accuracy for 2-D OCT slices, and by about 3.5% in area accuracy for 3-D OCT volumes.

Another limitation is in dealing with peripapillary atrophy. Because of the surrounding structure/tissue changes of the layer representing the RPE-choriocapillaris complex [38], [39], the RPE endpoints may be detected erroneously at the margin of the peripapillary atrophy with our technique. This challenging problem would also lead to failure of other optic disc detection methods. How to deal with peripapillary atrophy is an important direction for future work.

IV. CONCLUSION

In this paper, we have proposed a method for detecting the optic disc in a single OCT slice. Our method takes advantage of

the low-rank appearance structure and smooth shape variation along the RPE to identify the RPE endpoints that bound the optic disc. The low-rank dictionary discovers the intrinsic appearance structure of the RPE layer from training data that may contain outlier elements such as heavy noise and vessel shadows. Through a combination of low-rank reconstruction errors and a prior on RPE shape, the transition from RPE to optic disc can be detected with high accuracy in comparison to the current state-of-the-art methods. Moreover, our approach can also be employed to handle 3-D OCT volumes, for which promising results are also achieved.

REFERENCES

- [1] A. Manassakorn *et al.*, "Comparison of retinal nerve fiber layer thickness and optic disk algorithms with optical coherence tomography to detect glaucoma," *Amer. J. Ophthalmol.*, vol. 141, no. 1, pp. 105–115, 2006.
- [2] B. Chauhan and C. Burgoyne, "From clinical examination of the optic disc to clinical assessment of the optic nerve head: A paradigm change," *Amer. J. Ophthalmol.*, vol. 156, no. 2, pp. 218–227, 2013.
- [3] S. Yousefi *et al.*, "Glaucoma progression detection using structural retinal nerve fiber layer measurements and functional visual field points," *IEEE Trans. Biomed. Eng.*, vol. 61, no. 4, pp. 1143–1154, Apr. 2014.

- [4] M. Foracchia *et al.*, "Detection of optic disc in retinal images by means of a geometrical model of vessel structure," *IEEE Trans. Med. Imag.*, vol. 23, no. 10, pp. 1189–1195, Oct. 2004.
- [5] J. Xu *et al.*, "Automated optic disk boundary detection by modified active contour model," *IEEE Trans. Biomed. Eng.*, vol. 54, no. 3, pp. 473–482, Mar. 2007.
- [6] Y. Zheng *et al.*, "Optic disc and cup segmentation from color fundus photograph using graph cut with priors," in *Proc. Med. Imag. Comput. Comput. Assist. Intervent.*, 2013, pp. 75–82.
- [7] Y. Xu *et al.*, "Reconstruction-based optic cup localization for glaucoma screening," in *Proc. Med. Imag. Comput. Comput. Assist. Intervent.*, 2013, pp. 445–452.
- [8] J. Cheng *et al.*, "Superpixel classification based optic disc and optic cup segmentation for glaucoma screening," *IEEE Trans. Med. Imag.*, vol. 32, no. 6, pp. 1019–1032, Jun. 2013.
- [9] J. Xu *et al.*, "Optic disk feature extraction via modified deformable model technique for glaucoma analysis," *Pattern Recog.*, vol. 40, no. 7, pp. 2063–2076, 2007.
- [10] S. Morales *et al.*, "Automatic detection of optic disc based on PCA and mathematical morphology," *IEEE Trans. Med. Imag.*, vol. 32, no. 4, pp. 786–796, Apr. 2013.
- [11] W. Drexler and J. G. Fujimoto, "State-of-the-art retinal optical coherence tomography," *Prog. Retinal Eye Res.*, vol. 27, no. 1, pp. 45–88, 2008.
- [12] G. Jaffe and J. Caprioli, "Optical coherence tomography to detect and manage retinal disease and glaucoma," *Amer. J. Ophthalmol.*, vol. 137, no. 1, pp. 156–169, 2004.
- [13] A. Manassakorn *et al.*, "Comparison of optic disc margin identified by color disc photography and high-speed ultrahigh-resolution optical coherence tomography," *Arch. Ophthalmol.*, vol. 126, no. 1, pp. 58–64, 2008.
- [14] A. Reis *et al.*, "Influence of clinically invisible, but optical coherence tomography detected, optic disc margin anatomy on neuroretinal rim evaluation," *Invest. Ophthalmol. Visual Sci.*, vol. 53, no. 4, pp. 1852–1860, 2012.
- [15] M. Abràmoff *et al.*, "Automated segmentation of the cup and rim from spectral domain OCT of the optic nerve head," *Invest. Ophthalmol. Visual Sci.*, vol. 50, no. 12, pp. 5778–5784, 2009.
- [16] Z. Hu *et al.*, "Automated segmentation of neural canal opening and optic cup in 3D spectral optical coherence tomography volumes of the optic nerve head," *Invest. Ophthalmol. Visual Sci.*, vol. 51, no. 11, pp. 5708–5717, 2010.
- [17] H. Ishikawa *et al.*, "Automated assessment of optic nerve head with spectral domain optical coherence tomography," U.S. Patent 7 992 999, Aug. 9, 2011.
- [18] K. Lee *et al.*, "Segmentation of the optic disc in 3-D OCT scans of the optic nerve head," *IEEE Trans. Med. Imag.*, vol. 29, no. 1, pp. 159–168, Jan. 2010.
- [19] M. Miri *et al.*, "Multimodal segmentation of optic disc and cup from stereo fundus and SD-OCT images," *Proc. SPIE, Soc. Photo-Opt. Instrum. Eng.*, vol. 8669, Mar. 2013, pp. 1–8.
- [20] K. Boyer *et al.*, "Automatic recovery of the optic nerve head geometry in optical coherence tomography," *IEEE Trans. Med. Imag.*, vol. 25, no. 5, pp. 553–570, May 2006.
- [21] S. Lu *et al.*, "Automated layer segmentation of optical coherence tomography images," *IEEE Trans. Biomed. Eng.*, vol. 57, no. 10, pp. 2605–2608, Oct. 2010.
- [22] P. Dufour *et al.*, "Graph-based multi-surface segmentation of OCT data using trained hard and soft constraints," *IEEE Trans. Med. Imag.*, vol. 32, no. 3, pp. 531–543, Mar. 2013.
- [23] Y. Zheng *et al.*, "A generative model for oct retinal layer segmentation by integrating graph-based multi-surface searching and image registration," in *Proc. Med. Imag. Comput. Comput. Assist. Intervent.*, 2013, pp. 428–435.
- [24] N. Otsu, "A threshold selection method from gray-level histograms," *IEEE Trans. Syst., Man Cybern.*, vol. SMCA-9, no. 1, pp. 62–66, Jan. 1979.
- [25] W. Pratt, *Digital Image Processing*. New York, NY, USA: Wiley, 1978.
- [26] R. Spaide and C. Curcio, "Anatomical correlates to the bands seen in the outer retina by optical coherence tomography: Literature review and model," *Retina*, vol. 31, no. 8, pp. 1609–1619, 2011.
- [27] J. Jonas *et al.*, "Optic disc, cup and neuroretinal rim size, configuration and correlations in normal eyes," *Invest. Ophthalmol. Visual Sci.*, vol. 29, no. 7, pp. 1151–1158, 1988.
- [28] H. Quigley *et al.*, "The size and shape of the optic disc in normal human eyes," *Arch. Ophthalmol.*, vol. 108, no. 1, pp. 51–57, 1990.
- [29] E. J. Candès *et al.*, "Robust principal component analysis?" *J. ACM*, vol. 58, no. 3, pp. 1–37, 2011.
- [30] G. Liu *et al.*, "Robust recovery of subspace structures by low-rank representation," *IEEE Trans. Pattern Anal. Mach. Intell.*, vol. 35, no. 1, pp. 171–84, Jan. 2013.
- [31] Z. Lin *et al.*, "The augmented lagrange multiplier method for exact recovery of corrupted low-rank matrices," arXiv, pp. 1–23, 2010.
- [32] G. Golub and C. V. Loan, *Matrix Computations*. Baltimore, MD, USA: The Johns Hopkins Univ. Press, 1996.
- [33] T. Ojala *et al.*, "Multiresolution gray-scale and rotation invariant texture classification with local binary patterns," *IEEE Trans. Pattern Anal. Mach. Intell.*, vol. 24, no. 7, pp. 971–987, Jul. 2002.
- [34] S. John *et al.*, "Choice of cell source in cell-based therapies for retinal damage due to age-related macular degeneration: A review," *J. Ophthalmol.*, vol. 2013, pp. 1–9, 2013.
- [35] A. Fitzgibbon *et al.*, "Direct least square fitting of ellipses," *IEEE Trans. Pattern Anal. Mach. Intell.*, vol. 21, no. 5, pp. 476–480, May 1999.
- [36] D. Broadway *et al.*, "Optic disk appearances in primary open-angle glaucoma," *Survey Ophthalmol.*, vol. 43, pp. 223–243, 1999.
- [37] M. Fingeret *et al.*, "Five rules to evaluate the optic disc and retinal nerve fiber layer for glaucoma," *Optometry, J. Amer. Optometric Assoc.*, vol. 76, no. 11, pp. 661–668, 2005.
- [38] J. Jonas *et al.*, "Glaucomatous parapapillary atrophy: Occurrence and correlations," *Arch. Ophthalmol.*, vol. 110, no. 2, pp. 214–222, 1992.
- [39] V. Manjunath, *et al.*, "Analysis of peripapillary atrophy using spectral domain optical coherence tomography," *Ophthalmology*, vol. 118, no. 3, pp. 531–536, 2011.

Authors' photographs and biographies not available at the time of publication.